Spatial and Temporal Analysis of Urban Heat Island Effects in College of Science and Technology

Sangey Pasang[1], Chhimi Gembo*[2], Tandin Choki[3], Pema Choki Dorji[4], Thinley Namgay[5], Rigzin Norbu[6]

Civil Engineering Department, College of Science and Technology, Royal University of Bhutan
E-mail: sangeypasang.cst@rub.edu.bt[1], gembochhimi2035@gmail.com*[2], tandinchoki2001@gmail.com[3], pemachokeyy0230@gmail.com[4], thinleynamgay17658002@gmail.com[5], rigzinnorbu.cst@rub.edu.bt[6]

Received: 14 April 2025; Revised: 9 June 2025; Accepted: 12 July 2025; Published: 17 August 2025

Abstract
The phenomenon of Urban Heat Island (UHI) which is defined by increasing surface and air temperature in urban areas compared to surrounding areas is a growing concern due to several impacts. These includes heat stress, increase in energy consumption, degradation in environmental quality among others. Understanding the spatial and temporal variation of UHI will be useful in the planning of urban infrastructures. Therefore, the aim of the present study is to analyze the spatial and temporal variations of UHI in the College of Science and Technology (CST) from 2013 to 2023. The study analyzed the changes in Land Surface Temperature (LST), Normalized Difference Vegetation Index (NDVI) and Normalized Difference Built-up Index (NDBI). Air temperature was recorded at multiple locations at 8 AM, 12 PM and 4 PM over four days to examine the variation in air temperature due to the type of ground surface using handheld thermometer. The findings of the study show that there was a 3.5% increase in built-up area and a 17.14% decrease in vegetation cover during the 10-year period. The lower and upper limit of LST decreased over the decade which may be attributed to different seasonal timing. Normalized LST (NLST) analysis revealed that UHI zones expanded from 46.7% in 2013 to 53.3% in 2023. A weakening negative correlation between NDVI and LST (from -0.65 to -0.52) and a strengthening positive correlation between NDBI and LST (from 0.58 to 0.60) were observed, highlighting the cooling effect of vegetation and the heat retention of built-up surfaces. Air temperature patterns showed consistently higher values over built-up areas and cooler, more stable temperatures over vegetated zones. The findings provide valuable insight into the extent of the UHI effect in CST.
Key Words: *Urban Heat Island, Land Surface Temperature, NDVI, NDBI*

1. INTRODUCTION

Urbanization is an increase in the proportion of the population living in cities and the physical expansion of already existing urban centers (Tesfamariam et al., 2023). It is projected that almost 70% of the world's population will reside in urban areas by the year 2050 (UN Department of Economic and Social Affairs, 2019). In the recent decades rapid urbanization has caused a series of environmental problems owing to increased impervious layers and this trend is continuing, especially in developing regions such as Asian and sub-Saharan African countries (Parnell & Walawege, 2011). The environmental impacts caused by urbanization would include increased air pollution, water pollution and one of the major impacts being urban heat island (UHI) effects.

Urban Heat Island (UHI) refers to the higher temperatures experienced in urban areas compared to nearby non-urban areas (Rizwan et al., 2008). The UHI effect causes urban areas to experience higher temperatures than their rural counterparts due to various factors, including radiation absorption, decreased sky view, and increased anthropogenic heat sources (Roth et al., 1989). The diverse causes of UHI includes increased LST due to increase in population, high density of built spaces, impervious surface area (concrete structures, asphalt-paved roads and metal surfaces), reduced vegetation and air flow resulting in harmful climatic effects like less heat convections, evaporation, nocturnal radiation and albedo (Mahanta & Samuel, 2020).

In the past decades more than 120,000 people have died due to extreme heat in Europe and Russia, 75% of which occurred in cities (World Meteorological Organization, 2013); many thousands more were exposed to heat stress. Heat stress occurs when the human body's means of regulating its internal temperature starts to fail (Verdonck et al., 2018). UHI effect impacts on the development of meteorological events such as increased precipitation, boosts energy demands, poses threats to environmental quality and long-term sustainability of localities, and potentially contributes to global warming

(Kikegawa et al., 2006).

Numerous studies have explored the spatial and temporal dynamics of UHI, employing various methodologies to assess its impacts. Traditional approaches have relied heavily on satellite data, such as those from NASA (National Aeronautics and Space Administration) and NOAA (National Oceanic and Atmospheric Administration), to monitor LST and identify UHI hotspots (Gallo et al., 1993). LST can be measured directly or estimated through various remote sensing techniques such as Landsat, MODIS (Moderate Resolution Imaging Spectroradiometer), and ASTER (Advanced Spaceborne Thermal Emission and Reflection Radiometer) (Li et al., 2023).

UHI phenomena is divided into two distinct types: Surface Urban Heat Island (SUHI) and Atmospheric Urban Heat Island (AUHI). SUHI is the phenomenon where the urban areas emit higher land surface temperature compared to their rural surroundings. Factors which are contributing to SUHI include human activities, modification of land surfaces and replacement of vegetation by impervious surfaces (asphalt and concrete) which absorbs and retains more heat. The presence of infrastructures and buildings also reduces the flow of wind resulting in an increase of heat retention in urban areas (Oke, 1982).

AUHI is the phenomenon in which the air temperature in urban areas is higher compared to its surrounding rural areas. This occurs due to the high density of buildings and infrastructure which absorb and retain heat during the day and release slowly during the night. AUHI is further divided into two components: Canopy Layer Urban Heat Island (CLUHI) and Boundary Level Urban Heat Island (BLUHI).

The phenomenon in which the temperature of the air within the urban canopy layer that extends from the ground surface to the top of the buildings and trees is higher compared to the surrounding rural areas is known as Canopy Layer Urban Heat Island (CLUHI). The urban canopy layer is directly influenced by the characteristics of the urban surfaces and morphology of the buildings and vegetation (Oke, 1982). The effect of CLUHI is more noticeable at night because the urban area cools more slowly compared to rural areas.

BLUHI refers to the phenomenon in which the air temperature in the urban boundary layer that extends from top of the canopy layer to the level which is unaffected by surface heating is higher compared to the rural areas (Oke, 1982). The boundary later can extend hundreds of meters above the ground and is influenced by the characteristics of urban surface, anthropogenic heat emissions and the complex urban morphology. The presence of buildings and other infrastructures in urban areas will disturb the natural wind patterns, resulting in a thicker and warmer boundary level compared to rural areas (Oke, 1982).

In this study, the spatial and temporal patterns of Urban Heat Island (UHI) effects within the CST area are analyzed, focusing on both SUHI and AUHI phenomena. This analysis will be based on Land Use Land Cover (LULC), LST, and air temperature measurements. The specific objectives are to (1) generate LULC maps and assess temporal changes in land use (2) map LST and UHI to understand the spatial distribution of surface heat patterns; (3) analyze the relationship between LST, NDVI, NDBI and (4) determine and analyze air temperature variation.

2. STUDY AREA

The College of Science and Technology (CST) is located at approximately 26.85° N latitude and 89.39° E longitude, at an altitude of about 434 meters (1,424 feet) above sea level. It is characterized by a subtropical climatic zone, featuring distinct seasonal variations with warm summers and mild winters. Phuentsholing receives approximately 500-100 mm rainfall annually, primarily during the monsoon season from June to September (Phuentsholing Thromde, 2013).

3. METHODOLOGY

3.1. Data Collection

a. Landsat Images

Landsat is a series of Earth-observing satellite missions jointly managed by NASA and the United States Geological Survey (USGS). Although Landsat images can be freely downloaded from the United States Geological Survey (USGS) Earth Explorer for free, we were not able to find Landsat images taken on same day of the year. The Landsat images with a spatial resolution of 30 meters were selected from Landsat 8 with cloud cover less than 10 %. Even though image selected on 9th November, 2023 has 26.18 % cloud cover, the cloud does not cover the study area. This date was selected due to its proximity to 12 October 2013 as shown in

Table 1.

Table 1: *The Landsat data used in the study.*

Date	Path	Row	Cloud cover
12-10-2013	138	41	3.52
09-11-2023	138	41	26.18

b. Air Temperature Measurement

The measurement of air temperature was conducted to determine atmospheric urban heat island. The air temperature was measured using a handheld HT-9815 thermocouple thermometer, which has a least count of 0.1°C. The location of temperature measurement points was spread across the study area, encompassing all the different types of ground surface as shown in Fig. 1. The points 1, 3, 8 and 10 fall under built-up land whereas points 2, 7, 9 and 11 is under vegetation land type. The points 4 and 5 is under barren land type while the point 6 fall under waterbodies.

Fig. 1: *Location of air temperature measurement*

The thermometer was positioned at standard meteorological heights, typically between 1.5 to 2 meters above ground level while taking readings. This height ensures that the temperature data is consistent with established measurement protocols and minimizes the impact of ground-level effects that could distort the data (Rivera et al., 2023).

The collection of air temperature was done at 8 AM, 12 PM and 4PM. The timing was chosen based on the strength of the solar radiation in the study area. The early morning reading at 8 AM provides a baseline temperature before the sun's intensity reaches its maximum. The midday reading at 12 PM corresponds to the peak solar radiation period, when temperatures are expected to be at their highest. The late afternoon reading at 4 PM captures the temperature as solar radiation begins to decline, allowing for observation of temperature trends after the peak period. The collection of temperature across the study area was completed within 30 minutes. By collecting data at these specific times, the study aims to effectively capture the diurnal temperature variations influenced by solar radiation and identify potential UHI effects.

3.2. Data preparation and analysis

a. Preprocessing

The Landsat satellite records the energy reflected by the land and stores them as Digital Number (DN). DN is a variable assigned to a pixel in the form of a binary integer in the range of 0 to 4095 for Landsat 8. The raw data recorded by the sensor includes the radiation reflected from the surface, radiation that bounces in from neighboring pixels and the radiation reflected from clouds. The DN will not show the true surface temperature due to the disruption caused by the atmosphere and method of recording the data in the satellite. Therefore, the following steps are standard processing for TIRS band 10 before computing land surface temperature.

Conversion of DN to Top of Atmosphere (TOA) spectral radiance

Since DN cannot directly produce the temperature value, it needs to be converted to spectral radiance. According to Avdan & Jovanovska (2016) the top of atmosphere spectral radiance (L λ) is calculated using equation 1.

$$L\lambda = ML * Qcal + AL \qquad (1)$$

Where $L\lambda$ is the TOA spectral radiance ($Watts/(m^2 * srad * \mu m)$); ML is the band specific multiplicative rescaling factor from the metadata (radiance_multi_ban_x, where x is the band number), $Qcal$ is the quantized and calibrated standard product pixel values (DN) which is band 10 (thermal band) for Landsat 8 and AL is the band specific additive rescaling factor from the metadata (radiance_add_band_x, where x is the band number)

Conversion of TOA spectral radiance to At-Sensor Temperature (Kelvin)

The data need to be converted to brightness temperature using equation 2 (Avdan & Jovanovska, 2016).

$$TK = K_2/(ln\left(\frac{K_1}{L\lambda}\right) + 1) \qquad (2)$$

where TK is the At-sensor Temperature (K); K1 and K2 are band-specific thermal conversion constants from the metadata (K1 or

K2 _constant_band_x, where x is the thermal band number).

Conversion of temperature in Celsius

The result obtained in step 2 is in Kelvin and is changed into Celsius using equation 3.

$$TC = TK - 273.15 \qquad (3)$$

where TC is the At-sensor Temperature ($°C$).

b. Land Surface Temperature (LST) and Normalized LST computation

The Land Surface Temperature is calculated using the following steps:

Generation of Normalized Difference Vegetation Index (NDVI).

The NDVI assists in detecting the vegetated areas and evaluating the vegetation status (Cetin et al., 2024). The visible and near-infrared bands were used for calculating NDVI (Avdan & Jovanovska, 2016). The NDVI can be used to compute emissivity of the soil and vegetation. It can be computed using equation 4.

$$NDVI = (NIR - RED)/(NIR + RED) \qquad (4)$$

where NIR is the near-infrared band (band 5) and RED is the red band (band 4).

Computation of Vegetation Proportion (PV)

The vegetation proportion is highly related to NDVI and emissivity. It is calculated using equation 5.

$$PV = \left(\frac{(NDVI - NDVI_{min})}{(NDVI_{max} - NDVI_{min})}\right)^{\frac{1}{2}} \qquad (5)$$

where $NDVI_{min}$ and $NDVI_{max}$ are the minimum and maximum values obtained in the $NDVI$ calculation respectively.

Emissivity estimation

Since the land surface emissivity is a proportionality factor that scales blackbody radiance to predict emitted radiance, it must be computed to estimate LST (Avdan & Jovanovska, 2016). De Almeida et al. (2021) suggested equation 6 to estimate emissivity (E).

$$E = 0.004 * PV + 0.986 \qquad (6)$$

Computation of LST

The LST can be computed using equation 7 (Avdan & Jovanovska, 2016).

$$LST = (TC/(1 + \left(\lambda * \frac{TC}{\rho}\right) * ln\,(E) \qquad (7)$$

Where LST is the temperature, with correction by emissivity ($°C$); LC is the temperature of the brightness at the sensor ($°C$); λ is the wavelength of the emitted radiance; E is the emissivity; ρ is which is deduced from equation 8.

$$\rho = h\,\frac{c}{\sigma} = (1.428 * 10^{-2}\ mk) \qquad (8)$$

Where σ is the Boltzmann constant ($1.38 * 10^{-23}\ J/K$); h is Planck's constant ($6.626 * 10^{-34}\ Js$), and c is the speed of light ($2998 * 10^{8}\ m/s$).

Normalized Land Surface Temperature (NLST)

It is not appropriate to directly compare LST due to seasonal variation and inter-annual climatic variability. Therefore, LST maps need to be normalized using equation 9 before conducting quantitative analysis (Yang et al., 2017).

$$NLST = \frac{LST_i - LST_{min}}{LST_{max} - LST_{min}} \qquad (9)$$

Where $NLST$ is the normalized LST value of pixel i; LST_i is the initial LST of pixel i; LST_{max} and LST_{min} are the maximum and minimum LST respectively.

3.3. Normalized Difference Built-up Index (NDBI)

The NDBI is an essential index to detect built-up areas. It is obtained by dividing the difference between the spectral reflectance of short-wave infrared (SWIR) and NIR (Near Infrared) band values by their sum (Cetin et al., 2024). NDVI values range from +1 to -1 where positive value indicate built-up areas and negative value indicate non-urban areas. It is calculated using the formula in equation 9.

$$NDBI = \frac{(SWIR\ BAND - NIR\ BAND)}{(SWIR\ BAND + NIR\ BAND)} \quad \ldots (9)$$

Where SWIR and NIR are the Shortwave Infrared and Near-Infrared band respectively.

3.4. Land Use Land Cover (LULC)

Land cover represents the physical and natural characteristics of the Earth's surface, including vegetation, soil, water, and other elements. In contrast, land use refers to the human alterations of land cover for purposes such as industry, settlement, and commerce (Kaul & Sopan, 2012).

To understand the spatial variations in land cover and land use, LULC maps are prepared by manually digitizing the land cover due to small study area and coarse spatial resolution of Landsat. This process involves creating a shapefile of the study area and classifying it into

four primary land classes: Built-up (urban areas, commercial zones, roads, pavements, and other man-made structures), Vegetation (forests, agricultural fields, parks, grasslands, and meadows), Barren (sand, gravel, rocks, and riverbanks), and Water (rivers, lakes, and streams).

3.5. LULC validation

To validate the LULC maps, their accuracy is assessed by comparing the land classes identified on the maps with the actual land classes observed in the field. This process involves randomly selecting multiple points from the LULC maps, recording their coordinates, and inputting these coordinates into Google Earth Pro. We have used historical image which are obtained in Google Earth Pro. The land classifications observed in the high-resolution satellite images from Google Earth Pro are then compared with those on the LULC maps using confusion matrix. This comparison aims to determine the accuracy of the land classifications by evaluating the proportion of correctly predicted land types, thus ensuring the reliability of the LULC maps.

4. RESULT AND DISCUSSION

4.1. Land use land cover dynamics

The Table 2 and 3 indicates that from 2013 to 2023, the built-up area increased from 16,885 m² to 25,607 m², an increase of 3.5 % as percent of the total area. This could be due to the construction of the convention hall, hostel, and other land development activities. On the other hand, the vegetation and barren land areas has changed significantly, with vegetation decreasing by 17.13% and barren land increasing by 13.49%. Water bodies, which were not recorded in 2013, was found to have 300.95 m² in 2023 as shown in Table 3. This increase is due to the formation or identification of a pond in the study area. The location of each LULC classes in 2013 and 2023 are shown in Fig. 2 and 3 respectively.

Table 2: *LULC classification for 2013 and 2023*

Class	2013		2023	
	Area (m^2)	Area (%)	Area (m^2)	Area (%)
Built-up	16,885	9.62	25,607	13.12
Vegetation	124,465	70.92	104,973	53.78
Barren	34,160	19.46	64,312	32.95
Water	-	-	301	0.15

Table 3: *LULC Changes from 2013 to 2023*

Class	Change	
	Area (m^2)	Area (%)
Built-up	+8721.72	+3.50%
Vegetation	-19,492.06	-17.14%
Barren	+30,151.36	+13.49%
Water	+300.95	+0.15%

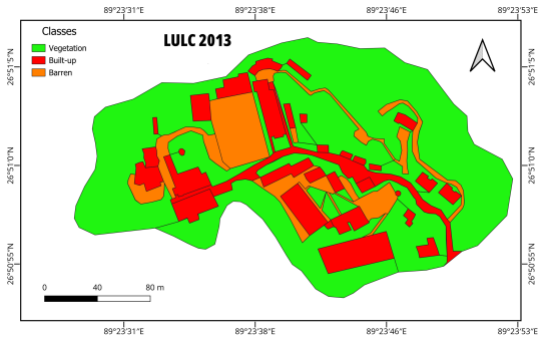

Fig. 2: *LULC map of 2013*

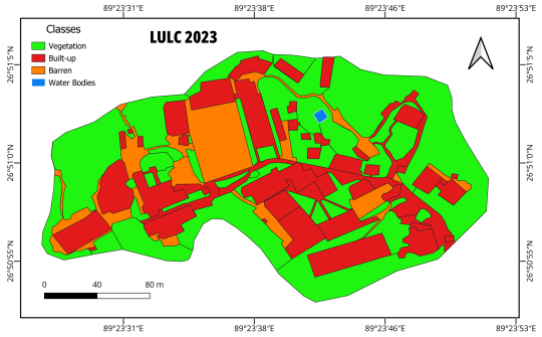

Fig. 3: *LULC map of 2023*

The point sampling method was used for assessing the assessment of the LULC maps for the year 2013 and 2023. A total of 120 points were selected for each year, proportionately distributed based on the percentage area of each land cover class as shown in Table 4. These points were then subjected to ground truthing and verification using field data and reference imagery, allowing for an effective comparison between the actual and classified land covers.

Table 4: *Sample point distribution*

Year	Class	Area (%)	Points
2013	Barren	19.46	23
	Vegetation	70.91	85
	Built-up	9.62	12
2023	Barren	13.12	16
	Vegetation	53.78	65
	Built-up	32.95	37

Water	0.0015	2

To assess the classification performance of the LULC maps for the years 2013 and 2023, a point-based accuracy assessment was conducted

coverage. These points were verified through reference imagery.

The overall classification accuracy of the LULC maps after a confusion matrix was 85.65 % for 2013 and 93.33% for 2023, as summarized in Table 5.

Table 5: *Overall accuracy of LULC maps*

Year	Correct Points	Total Points	Overall Accuracy (%)
2013	103	120	85.65
2023	112	120	93.33

4.2. NDVI and NDBI result

The NDVI and NDBI values were derived from Landsat with a spatial resolution of 30 x 30 meters. Due to small size of the study area, the coarse resolution of the raster data resulted in a limited number of pixels covering the study area. This led to pixel misalignments as the pixel grid does not align perfectly with study area boundary.

The Fig. 4 and 5 shows the NDVI maps of CST for year 2013 and 2023 respectively. The areas with dense vegetation and sparse vegetation are represented by higher NDVI value, whereas lower values suggest less productive zones such as waterbodies, built-up areas and baren lands (Ahmad et al., 2025). The higher intensity of green colour indicates high NDVI value while lower NDVI are represented by increasing intensity of red colour. The calculated NDVI value varies from 0.05 and 0.46 in year 2013 while in year 2023 it varies from 0.09 to 0.42.

The high NDVI in 2013 are scattered across northeast and west of the study area whereas, the low NDVI are concentrated in the central area. In 2023, low NDVI areas are spread evenly with decreasing high NDVI areas, indicating decline in vegetation health and density.

using a stratified random sampling approach. A total of 120 sample points were selected for each year, proportionally distributed across land cover classes based on their area

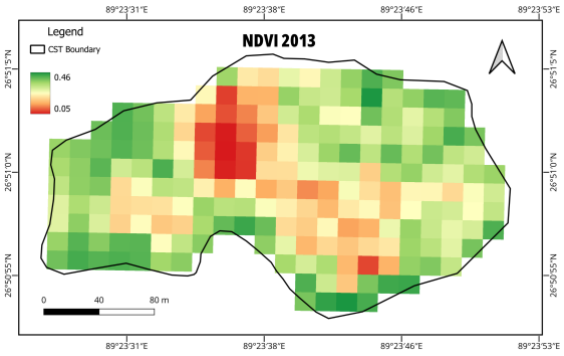

Fig. 4: *NDVI for 2013*

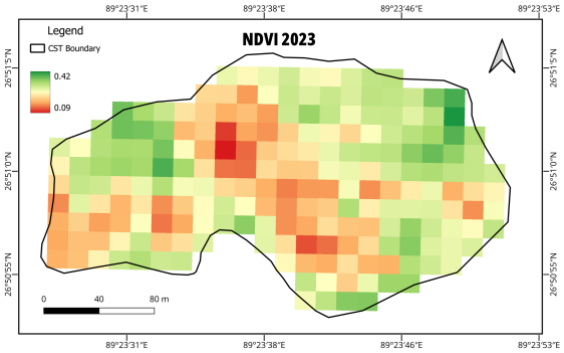

Fig. 5: *NDVI for 2023*

The Fig. 6 and 7 shows the NDVI maps of CST for year 2013 and 2023 respectively. High NDBI value represents built-up lands such as building and pavements and low NDVI value suggest presence of low-built up areas. The NDVI values for 2013 ranges from -0.27 to 0.17 whereas in 2023, it ranges from -0.25 to 0.14. The high values of NDVI are indicated by higher intensity of purple colour in the map and vice versa. The distribution of high NDVI values exhibits similar pattern to that of low NDVI indicating the increase of built-up area from 2013 to 2023.

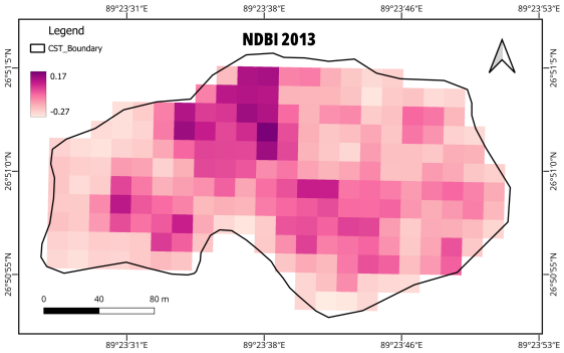

Fig. 6: *NDBI for 2013*

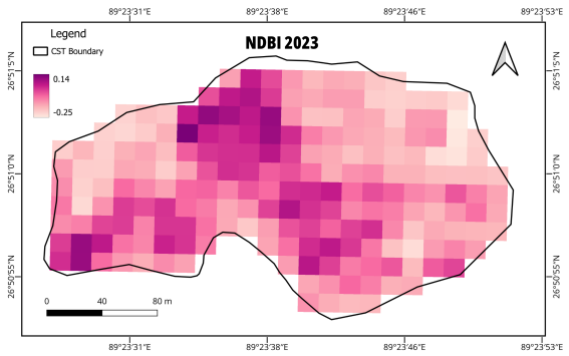

Fig. 7: *NDBI for 2023*

4.3. Land surface temperature and urban heat island

The spatial distribution of LST of CST during the year 2013 and 2023 are indicated by Fig. 8 and 9 respectively. The color gradient form light to deep green represents cooler areas while light to dark red represents warmer locations. The estimated LST values ranged from 24.9 to 30°C in 2013 and 22.7 to 27.2°C in 2023. The decrease in the lower and upper limit of LST may be attribute to different seasonal timing. Even though both datasets are captured during the post-monsoon seasons, November (Landsat obtained for 2023) is generally cooler than October (Landsat obtained for 2013). As a reference, the National Center for Hydrology and Meteorology (NCHM) recorded a minimum and maximum air temperature of 24°C and 33°C on 12 October 2013, and 16°C and 30.5°C on 9 November 2023. However, this information is presented for context only and does not necessarily explain the variation in LST values.

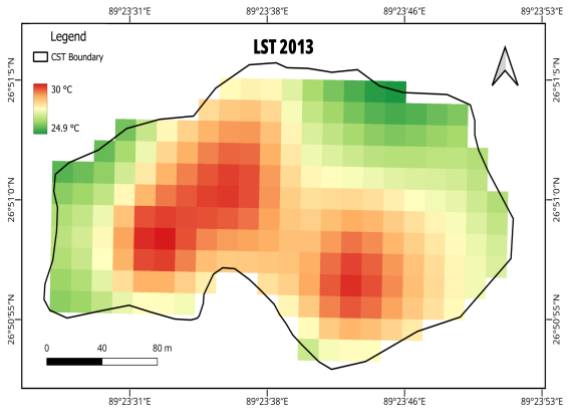

Fig. 8: *LST for 2013*

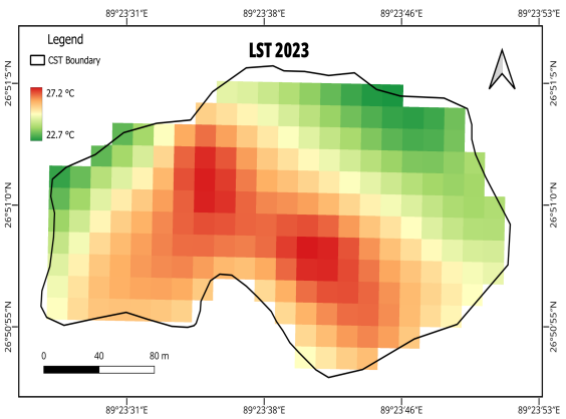

Fig. 9: *LST for 2023*

To account for seasonal variations and inter-annual variability of atmospheric conditions, normalization of LST is necessary. We classified normalized LST (NLST) equally in five zones with temperature ranges given in Table 6.

Table 6: *Temperature range for NLST zones*

Zone	Temperature
Very low temperature	$0 \leq NLST < 0.2$
Low temperature	$0.2 \leq NLST < 0.4$
Moderate temperature	$(0.4 \leq NLST < 0.6$
High temperature	$0.6 \leq NLST < 0.8$
Very high	$0.8 \leq NLST \leq 1$

The area where NLST is greater than or equal to 0.6 and less or equal to 1.0 ($0.6 \leq NLST \leq 1.0$) was defined as the UHI distribution zone (Xiong et al., 2012). Therefore, the combination of zone 4 and zone 5 was called the UHI distribution zone.

The Fig. 10 and 11 shows the zones of NLST of CST in 2013 and 2023. In 2013, the zone 1, zone 2, zone 3, zone 4 and zone 5 covers 7.55%, 20.28%, 25.47%, 29.25% and 17.45% of the total area respectively. The UHI zone which is the combination of zone 4 and 5 covers 46.75% of the area. While in 2023, the zone 1, zone 2, zone 3, zone 4 and zone 5 covers 10.38%, 16.51%, 19.81%, 30.66% and 22.64% of the total area respectively. The UHI zone which is the combination of zone 4 and 5 covers 53.3 % of the area.

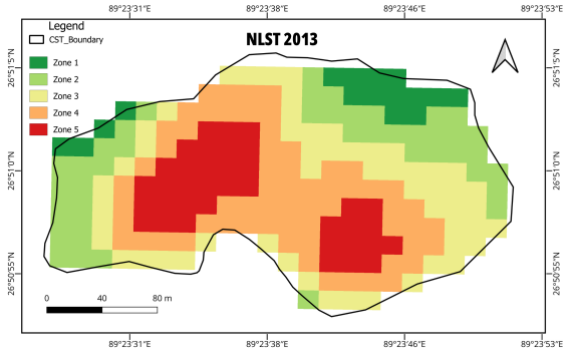

Fig. 10: *NLST for 2013*

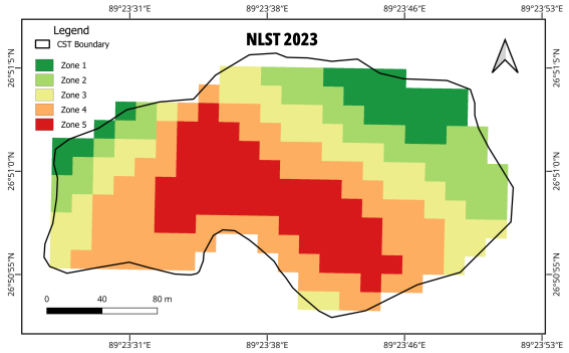

Fig. 11: *NLST for 2023*

In a decade, the area of very low temperature (zone 1) has increased by 2.83 %, the low temperature zone (zone 2) and moderate temperature zone (zone 3) has decreased by 3.77 % and 5.66 % respectively while high temperature zone (zone 4) and very high temperature zone (zone 5) has increased by 1.41 % and 5.19 % respectively as indicated in Table 7. Overall, the UHI zone has increased by 6.6 % over the decade.

Table 7: NLST zone details in 2013 and 2023

Zone	2013 Area		2023 area		Change
	m^2*	%	m^2*	%	%
1	14.4	7.55	19.8	10.38	2.83
2	38.7	20.28	31.5	16.51	-3.77
3	48.6	25.47	37.8	19.81	-5.66
4	55.8	29.25	58.5	30.66	1.41
5	33.3	17.45	43.2	22.64	5.19

*Area is in thousand meters square

The UHI zone (zone 4 and zone 5) are mostly located in the central area of CST in both year 2013 and 2023. These central areas include football ground, administration and academic buildings and hostel buildings. The two heat island in 2013 has combined into single large UHI zone in the 2023.

4.4. Correlation Analysis of LST and NDVI and NDBI

The Fig. 12 and 13 respectively shows the scatter plot between LST and NDVI for 2013 and 2023. From 2013 to 2023, the strength of the negative correlation between LST and NDVI decreased from -0.65 ($R^2 = 0.4194$) to -0.52 ($R^2 = 0.269$), indicating a weakening influence of vegetation on surface temperature moderation.

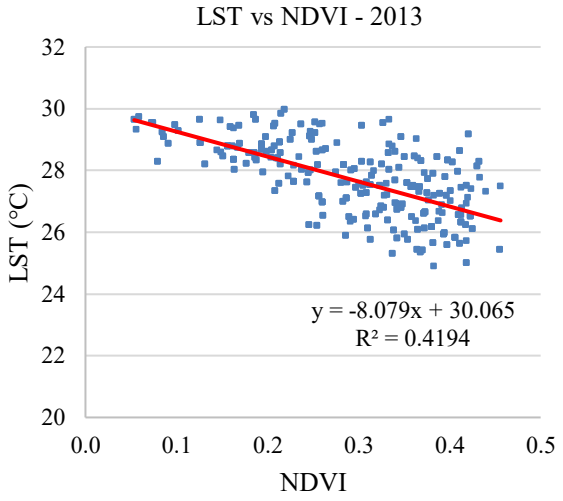

Fig. 12: Regression result between LST and NDVI in 2013

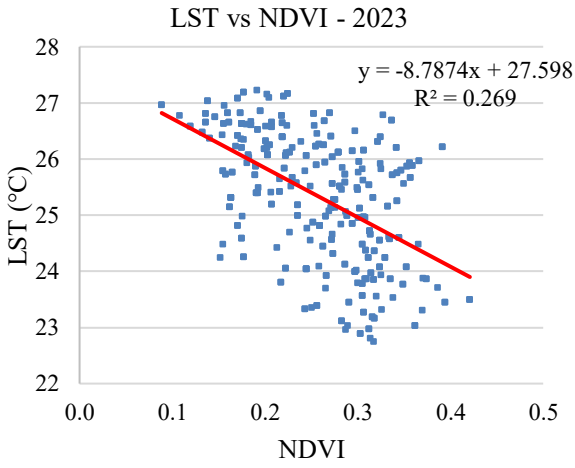

Fig. 13: Regression result between LST and NDVI in 2023

The Fig. 14 and 15 shows the scatter plot between LST and NDBI for 2013 and 2023 respectively. From 2013 to 2023, the strength of the positive correlation between LST and NDBI increased from 0.58 ($R^2 = 0.3351$) to 0.60 ($R^2 = 0.3556$), suggesting a growing influence of built-up areas on surface temperature.

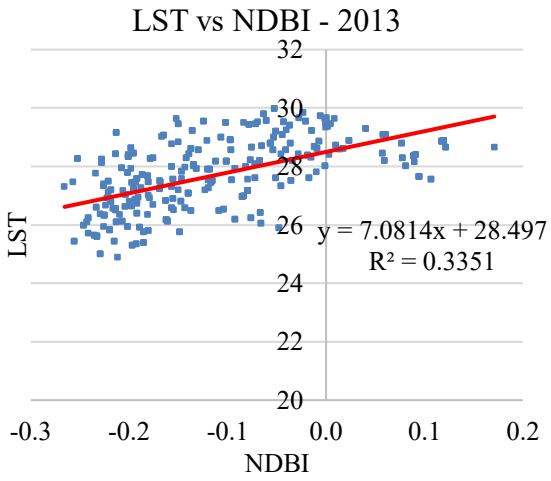

Fig. 14: *Regression result between LST and NDBI in 2013*

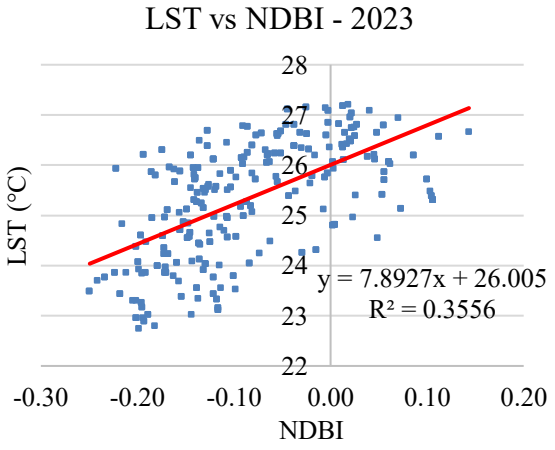

Fig. 15: *Regression result between LST and NDBI in 2023*

4.5. Variability of Air Temperature

Inverse Distance Weighting (IDW) interpolation method was employed in GIS to estimate the air temperature at the unmeasured location based on known values at surrounding point of the study area. In IDW, points closer to the location being estimated have a greater influence on the interpolated value, while points farther away have less influence. This allows us to generate spatial heat maps as shown in Fig. 16.

The heat hotspots were not uniform with different areas showing greater temperature at different times. However, the hotspots were consistently in the built-up area throughout the study period, indicating the influence of structures and their material on ambient temperature. The ambient temperatures around the vegetation areas are uniform and comparatively cool. Similarly, the air temperature over the barren land were not significantly hot. In built-up areas, there is a higher proportion of impervious surfaces (such as pavements, roads, and buildings) that absorb, and store heat more readily compared to natural surfaces. These areas also have darker surfaces that absorbs more solar radiation.

5. CONCLUSION

The study highlighted the presence and evolution of UHI effects on CST campus over a decade from 2013 to 2023. The LST analysis showed a spatial concentration of heat in built-up and barren areas. Although a reduction in the LST over the decade was observed, the UHI zones expanded from 46.75% in 2013 to 53.3% in 2023.

The analysis revealed a weak negative correlation between NDVI and LST, emphasizing the role of vegetation in reducing surface temperatures. Meanwhile, the moderate

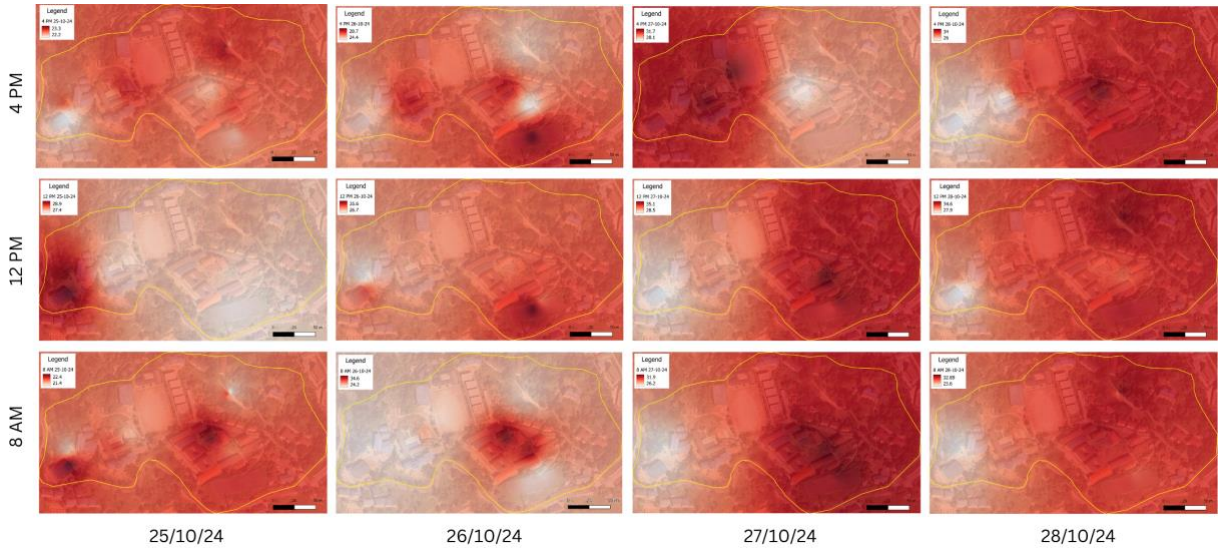

Fig. 16: *Air Temperature (in °C) variation across different time*

positive correlation between NDBI and LST demonstrated the heat-retaining characteristics of impervious surfaces.

Air temperature data reinforced the findings, consistently identifying heat hotspots in built-up regions, particularly during peak solar radiation periods. Conversely, vegetation-covered areas exhibited relatively stable and cooler temperatures, reaffirming the moderating role of green spaces

Overall, the findings indicate that increased construction activities at CST have contributed to an expansion in the spatial coverage of UHI zones. The findings highlight the necessity of preserving and integrating vegetation into the future development of the campus. Implementing measures like tree planting, vegetative buffer maintenance, and the use of permeable or reflective surface material can prove to be effective in mitigating UHI effects. This study provides localized information on how land use change at CST influences thermal patterns and can be utilized as a baseline to track the impact of future urbanization in comparable institutional or educational complexes in Bhutan.

REFERENCES

Ahmad, M., Saqib, M., Ahmad, S. N., Jamal, S., & Mir, A. Y. (2025). Normalized difference spectral indices and urban land cover as indicators of urban heat island effect: a case study of Patna Municipal Corporation. *Geology, Ecology, and Landscapes*, *00*(00), 1–21. https://doi.org/10.1080/24749508.2025.2451479

Avdan, U., & Jovanovska, G. (2016). Algorithm for automated mapping of land surface temperature using LANDSAT 8 satellite data. *Journal of Sensors*, *2016*, 8. https://doi.org/10.1155/2016/1480307

Cetin, M., Ozenen Kavlak, M., Senyel Kurkcuoglu, M. A., Bilge Ozturk, G., Cabuk, S. N., & Cabuk, A. (2024). Determination of land surface temperature and urban heat island effects with remote sensing capabilities: the case of Kayseri, Türkiye. *Natural Hazards*, *120*(6), 5509–5536. https://doi.org/10.1007/s11069-024-06431-5

De Almeida, C. R., Teodoro, A. C., & Gonçalves, A. (2021). Study of the urban heat island (Uhi) using remote sensing data/techniques: A systematic review. *Environments*, *8*(105), 1–39. https://doi.org/10.3390/environments8100105

Gallo, K. P., McNab, A. L., Karl, T. R., Brown, J. F., Hood, J. J., & Tarpley, J. D. (1993). The Use of NOAA AVHRR Data for Assessment of the Urban Heat Island Effect. *Journal of Applied Meteorology*, *32*(5), 899–908. https://doi.org/10.1175/1520-0450(1993)032<0899:TUONAD>2.0.CO;2

Kaul, H. a, & Sopan, I. (2012). Land Use Land Cover Classification and Change Detection Using High Resolution Temporal Satellite Data. *Journal of Environment*, *01*(04), 146–152.

Kikegawa, Y., Genchi, Y., Kondo, H., & Hanaki, K. (2006). Impacts of city-block-scale countermeasures against urban heat-island phenomena upon a building's energy-consumption for air-conditioning. *Applied Energy*, *83*(6), 649–668. https://doi.org/10.1016/j.apenergy.2005.06.001

Li, Z. L., Wu, H., Duan, S. B., Zhao, W., Ren, H., Liu, X., Leng, P., Tang, R., Ye, X., Zhu, J., Sun, Y., Si, M., Liu, M., Li, J., Zhang, X., Shang, G., Tang, B. H., Yan, G., & Zhou, C. (2023). Satellite Remote Sensing of Global Land Surface Temperature: Definition, Methods, Products, and Applications. *Reviews of Geophysics*, *61*(1), 1–77. https://doi.org/10.1029/2022RG000777

Mahanta, N. R., & Samuel, A. K. (2020). Study of Land Surface Temperature (LST) and Land Cover for Urban Heat Island (UHI) Analysis in Dubai. *ICRITO 2020 - IEEE 8th International Conference on Reliability, Infocom Technologies and Optimization (Trends and Future Directions)*, 1285–1288. https://doi.org/10.1109/ICRITO48877.2020.9198038

Oke, T. R. (1982). The energetic basis of the urban heat island (Symons Memorial Lecture, 20 May 1980). *QUARTERLY JOURNAL OF THE ROYAL METEOROLOGICAL SOCIETY*, *108*(455), 1–24. https://doi.org/https://doi.org/10.1002/qj.49710845502

Parnell, S., & Walawege, R. (2011). Sub-Saharan African urbanisation and global environmental change. *Global Environmental Change*, *21*(SUPPL. 1), S12–S20. https://doi.org/10.1016/j.gloenvcha.2011.09.014

Phuentsholing Thromde. (2013). *Phuentsholing Structure Plan -2013-2028 (Vol. 01): Vol. Vol. 01*.

Rivera, A., Ponce, P., Mata, O., Molina, A., & Meier, A. (2023). Local Weather Station Design and Development for Cost-Effective Environmental Monitoring and Real-Time Data Sharing. *Sensors*, *23*(22). https://doi.org/10.3390/s23229060

Rizawan, A. M., Dennis, L. Y. C., & Liu, C. (2008). A review on the generation, determination and mitigation of Urban Heat Island. *Journal of Environmental Sciences*, *20*(1), 120–128. https://doi.org/10.1016/S1001-0742(08)60019-4

Roth, M., Oke, T. R., & Emery, W. J. (1989). Satellite-derived urban heat islands from three coastal

cities and the utilization of such data in urban climatology. *International Journal of Remote Sensing*, *10*(11), 1699–1720. https://doi.org/10.1080/01431168908904002

Roy, D. P., Wulder, M. A., Loveland, T. R., C.E., W., Allen, R. G., Anderson, M. C., Helder, D., Irons, J. R., Johnson, D. M., Kennedy, R., Scambos, T. A., Schaaf, C. B., Schott, J. R., Sheng, Y., Vermote, E. F., Belward, A. S., Bindschadler, R., Cohen, W. B., Gao, F., … Zhu, Z. (2014). Landsat-8: Science and product vision for terrestrial global change research. *Remote Sensing of Environment*, *145*, 154–172. https://doi.org/10.1016/j.rse.2014.02.001

Tesfamariam, S., Govindu, V., & Uncha, A. (2023). Spatio-temporal analysis of urban heat island (UHI) and its effect on urban ecology: The case of Mekelle city, Northern Ethiopia. *Heliyon*, *9*(2), e13098. https://doi.org/10.1016/j.heliyon.2023.e13098

UN Department of Economic and Social Affairs. (2019). World Urbanization Prospects. In *Demographic Research* (Vol. 12). https://population.un.org/wup/Publications/Files/WUP2018-Report.pdf

Verdonck, M. L., Demuzere, M., Hooyberghs, H., Beck, C., Cyrys, J., Schneider, A., Dewulf, R., & Van Coillie, F. (2018). The potential of local climate zones maps as a heat stress assessment tool, supported by simulated air temperature data. *Landscape and Urban Planning*, *178*(July 2017), 183–197. https://doi.org/10.1016/j.landurbplan.2018.06.004

World Meteorological Organization. (2013). The Global Climate 2001-2010: a decade of climate extremes. WMO, No. 1103. In *WMO Publications Board* (Issue 1119). http://library.wmo.int/pmb_ged/wmo_1103_en.pdf

Xiong, Y., Huang, S., Chen, F., Ye, H., Wang, C., & Zhu, C. (2012). The Impacts of Rapid Urbanization on the Thermal Environment: A Remote Sensing Study of Guangzhou, South China. *Remote Sensing*, *4*(7), 2033–2056. https://doi.org/10.3390/rs4072033

Yang, C., He, X., Yan, F., Yu, L., Bu, K., Yang, J., Chang, L., & Zhang, S. (2017). Mapping the influence of land use/land cover changes on the urban heat island effect-A case study of Changchun, China. *Sustainability*, *9*(2), 17. https://doi.org/10.3390/su9020312